Instability Deposit Patterns in an Evaporating Droplet

3 **AUTHORS**, INCLUDING:

Chun Sang Yoo

Ulsan National Institute of Science and Techn…

56 PUBLICATIONS   **928** CITATIONS

SEE PROFILE

Instability Deposit Patterns in an Evaporating Droplet

Narina Jung,[†,‡] Chun Sang Yoo,*[†] and Perry H. Leo*[‡]

[†]School of Mechanical and Advanced Materials Engineering, Ulsan National Institute of Science and Technology, Ulsan 689-798, Republic of Korea

[‡]Aerospace Engineering and Mechanics, University of Minnesota, Minneapolis, Minnesota 55455, United States

ABSTRACT: The characteristics of several patterns left after the evaporation of a particle-laden liquid droplet are investigated by using a coarse-grained lattice model. The model includes both evaporative convection and the Brownian motion of weakly interacting particles. The model is implemented by using a Monte Carlo method to investigate the different deposit patterns near the contact line. It was found that different deposit patterns form depending on the interplay between the convective transport and the deposition of interacting particles. The patterns were analyzed by varying the ratio of the convective forces to the interaction forces as well as the size and the number of particles. It was also found that the ring-like patterns are formed when the convective potential dominates the interactions of particles, whereas either wave-like or island-like patterns form in the opposite case. Finally, the average thickness of the wave-like patterns is mainly determined by evaporation rates.

INTRODUCTION

Evaporative self-assembled patterns of particles on a substrate are commonly found in everyday life and are important in surface patterning techniques such as painting, coating, and printing.[1−3] Recently, as a nonlithography method of nanoparticle assemblies, evaporation-induced pattern formation has been applied to micro- and nanosystems, electronic devices and sensors, DNA/RNA microarrays, polymer printing and coating, drug delivery, etc.[4−10]

Evaporation-induced pattern formation has been investigated by Deegan and his co-workers, who found the "coffee-ring" effect, which is the formation of ring-like patterns left after the evaporation of a particle-laden liquid droplet.[11,12] The coffee-ring effect has been accounted for by capillary flow, which is induced by the evaporation and pinned contact line of a droplet. Different particles and solutions can make various deposit structures on substrates. Recently, wave-like deposit patterns of monodispersed dendrimer particles has been observed from the evaporation of a micrometer-size droplet.[13,14]

Most of the early work on evaporation induced pattern formation has focused on the control of the convective capillary flows to remove the coffee-ring effect. The characteristic scales of the systems in these studies are in general micrometers or above. For instance, Hu and Larson investigated the effect of Marangoni flows to suppress the "coffee-ring" phenomena in an evaporating sessile droplet.[15] The Marangoni flow reverses the capillary flow and leaves a homogeneous deposit. Denkov et al. found that the convective transport and the lateral attractive capillary forces of particles form two-dimensional crystal ordering in an evaporating liquid film.[16] Yunker et al. investigated the effect of the capillary interaction between particles by controlling the shape of particles. They found that the coffee-ring effect can be eliminated by the use of ellipsoidal particles.[17,18] The shape dependency of the evaporative deposit patterns suggests an application to biosensors to detect targeted molecules in a solution by simple evaporation.[14,19]

The effect of evaporation rate on the evaporative self-assembled structures has also been studied. Deegan investigated the effect of different evaporation rate on the growth of ring-like patterns by comparing two cases: diffusion-limited evaporation and uniform evaporation over a pinned droplet.[11] In the diffusion limited case, the evaporation rate diverges at the contact line and, hence, a thinner ring is formed compared to the uniform evaporation case. A minimal size of a droplet associated with the occurrence of the coffee-ring effect was reported by Shen et al.[20] They found that a droplet with size under a critical value ($\approx 1~\mu$m) leaves a uniform deposit because the Brownian motion of particles is the main mechanism to bring particles close to each other. On the other hand, ring-like patterns are observed in larger droplets where particles are mainly transported by convection. Cheng et al. showed by using a molecular simulation that a defect-free crystalline array of nanoparticles can be obtained by reducing the evaporation rate and thus speeding up the relative diffusion rate of nanoparticles.[21]

The dynamics of the pattern growth process have also been studied.[22−28] Rabani et al. explicitly introduced different types of evaporation in a coarse-grained lattice model and found various self-assembled structures of nanoparticles by coupling the dynamics of the solvent evaporation with the diffusional aggregation during the pattern forming process.[22] In their model, the transport of particles by convection was ignored because the time-scale of the Brownian motion is much smaller

than that of the convection of particles in the submicrometer scaled systems they considered.[28]

Recently, Li et al. experimentally obtained unique condensed-ring structures from drying micrometer-sized droplets.[13,14] They observed periodically scalloped dendrimer rings and found that their characteristic wavenumbers depend on the evaporation rates of alcohols, and the types and the concentration of dendrimer particles. The wave-like patterns are visually similar to the rim-instability patterns of the dewetting hole front of a liquid, which is a Rayleigh-type instability driven by the surface tension.[29−34] The wavenumber of the rim-instability is proportional to the rim width, with proportionality constant four, and is independent of liquid properties.

Due to the similarity of the wave-like patterns to the rim-instability, Li et al. investigated the relation between the wavenumbers and the averaged thickness of the wave-like deposit patterns. The relation is approximately linear and the proportionality depends on the types of solvent: for a pentanol based solution, it is 4.8 and for a hexanol based solution it is 2.3. To explain the different proportionality, they conjectured that surface tensions of the two solutions cause the different morphology. However, measurements of the surface tensions have proven inconclusive and the mechanism of wave-like pattern formation also remains unexplained.[13,14]

In this work, we explore that weak dispersion forces, together with the transport of dendrimer particles toward a contact line, can form wave-like patterns. The dendrimer particles are electrically neutral macromolecules with highly branched spherical shapes. Because of such tree-like structures at a nanometer scale, dendrimers have large surface areas and thus it can be expected that the dispersion interactions of nanoparticles will be important in the deposit patterns.

The objective of the present study is to investigate the underlying mechanism of the wave-like deposit pattern formation. We focus on the competition between the convective transport of particles and deposition process of the weakly attracting particles. For this purpose, we define a configurational Hamiltonian employing the coarse-grained lattice model proposed by Rabani and his co-workers.[22] The lattice model is an Ising-type lattice model developed to study the properties of the interacting spins of ferromagnets. The model is simulated by using the Monte Carlo method to find the equilibrium configuration of a system.[35] Unlike the Rabani model in which the convective transport of particles is ignored, we investigate cases in which particles in a drying droplet are mainly transported by the convection. To simulate such cases, we modify the lattice model to include both the convection and the interaction of nanoparticles. In addition, on the basis of a rough calculation that the Stokes number is order 10^{-15} for our system, we assume that particles are simple tracers of solvent. That is, particle motion is determined from the evaporation-driven dynamics of the solvent, which can be found analytically prior to the lattice model simulation. The underlying mechanism of the pattern formation is elucidated using three parameters: the ratio Q of convectional potential to interaction potential, the radius of particles R_M, and the total number of particles N_{tot} that affect the volume fractions of particles during deposition process. A detailed description of the model is given in the following section.

■ COARSE-GRAINED LATTICE MODEL

The present model uses two-dimensional lattice and assigns a configurational energy on each cell, H_ν, that describes a state of the particles distributed in an evaporating and convecting solvent. Using the Monte Carlo method, we compute the minimum value of H_ν to find an equilibrium configuration.

Circular Lattice. For effective simulations of particle evolution in a drying sessile droplet, we introduce a two-dimensional circular lattice of a substrate wetted by a droplet. In the grid system, the droplet radius R_0 is divided into n_0 different annular layers, where the width of one layer is given by $dr = R_0/n_0$ and each layer is divided into a number of cells whose areas are approximately $a_0 = dr^2$ (Figure 1). Although
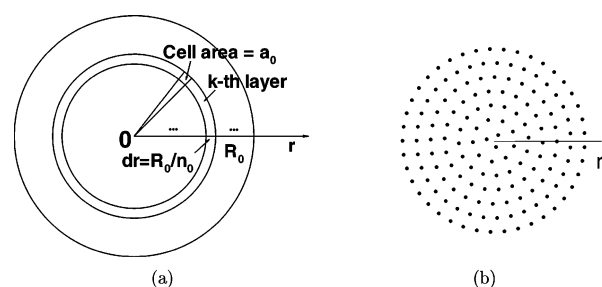

Figure 1. Schematic of the circular grid system adopted in the simulations. The layers and cells are shown in (a), and their arrangement as discretized nodes in (b).

the radial lattice is not common, it is more suitable for an axisymmetric droplet system to capture the radial behavior of particles transferring toward the contact line and the deposition process around the contact line at $r = R_0$. When a rectangular lattice is used instead of a circular one, spurious hexagonal aggregation patterns can be obtained in the simulation of ring-like patterns, which might be erroneous wave-like patterns.[36] In the present study, the formation of wave-like patterns of particles is investigated and as such, a circular lattice is adopted rather than a rectangular lattice.

The droplet is assumed to be a spherical cap with contact angle $\theta(t)$ that decreases during evaporation. Hence, assuming $\theta(t) \ll 1$, the droplet height can be approximated as

$$h(r,t) \approx \frac{R_0{}^2 - r^2}{2R_0}\theta(t)$$

The total number of particles N_{tot} is distributed in a droplet with initial volume V_0 corresponding to initial contact angle θ_0. Each site i of the circular lattice is occupied by N_i particles that move with evaporation induced velocity v_i. Also each site i has volume V_i that can be computed from the grid parameters and the droplet height. Each distribution of N_i particles over the lattice defines one configurational state ν, and the energy of any particular state, $\nu = \{N_i|V_i,v_i\}$, is given by our Ising-like Hamiltonian H_ν detailed below.

Configurational Hamiltonian. The Hamiltonian discretized on a circular lattice is given by

$$H_\nu = \sum_i f_i N_i + \sum_{\langle i,j \rangle} g_{ij} N_i N_j + \sum_{\langle i,j \rangle} D|N_i - N_j| \tag{1}$$

where f_i is an external convective field, g_{ij} is the strength of the interaction between two neighboring particles at i and j, respectively, and D is a potential energy per unit difference of

particle numbers in the neighboring cells. The last two sums in eq 1 are taken over nearest neighbors.

The energy f_i accounts for a convection of particles toward the contact line, and is computed as

$$f_i = 6\pi\eta_m R_M \sqrt{a_0} \sum_{k=i}^{n_0} v_k \tag{2}$$

where $a_0 = dr^2$ is the area of a cell, $v_k = v(r_k,t)$, and n_0 is the number of cells along r-direction. It is obtained from potential energy $f(r,t)$ for a particle of a radius R_M to resist the Stoke's drag force F_d due to a solvent flow with prescribed velocity v_i and viscosity of solvent η_m. In other words,

$$f = \int_r^{R_0} F_d \, dr$$

and

$$F_d = 6\pi\eta_m R_M v(r,t)$$

The velocity $v(r,t)$ is obtained from the evaporation rate of which functional form depend on rate-limiting step of the evaporation.[11] When the rate-limiting step is the mass flux across the liquid–vapor interface, the evaporation rate is a constant. On the contrary, when the limiting step is the diffusive relaxation of the vapor phase immediately above the droplet, the evaporation rate diverge at the contact line. For the two types of the evaporation, i.e., the spatially uniform and diffusion-limited evaporations, the analytical forms of the velocity fields are approximated as

$$v(r,t) = \frac{B}{6\pi}\left(\frac{h(0,t)}{R_0}\right)^{-\lambda(t)} \quad \text{and} \quad v(r,t) = \frac{B}{6\pi}\left(\frac{h(r,t)}{R_0}\right)^{-\lambda(t)} \tag{3}$$

respectively, where B is a constant that is proportional to the average evaporation rate, $\lambda(t) = (\pi - 2\theta(t))/(2\pi - 2\theta(t))$, and $\theta(t)$ is the contact angle which the liquid makes with the substrate at time t.[11] Figure 2 shows the temporal evolution of
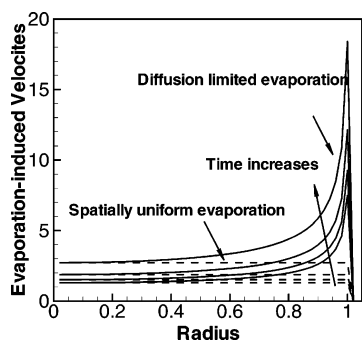

Figure 2. Temporal evolution of the profile of two different evaporation rates along the radius of the droplet: a diffusion-limited evaporation and a spatially uniform evaporation.

the velocity fields defined in eq 3. The velocities of the two cases are the same at the center of a droplet, where the boundary effects of different drying conditions at the contact lines are minimal. The evaporation rate diverges at the contact line in the diffusion limited case, whereas it is constant in the spatially uniform case. Velocities are discretized and are incorporated in the convective potential f_i (eq 2) and total Hamiltonian H_v (eq 1). Note the assumption that in

computating f_i particles passively follow the behavior of a solvent with a velocity $v(r,t)$, which is prescribed prior to the computations of the Hamiltonian at each time step.

The interaction energy between two neighboring cells are accounted for by g_{ij}:

$$g_{ij} = -\frac{C}{a_0 \overline{d}_{ij}^4} \tag{4}$$

where C is a dispersion constant, $\overline{d}_{ij} = (d_i + d_j)/2$, $d_i = (V_i/N_i)^{1/3}$, and $d_j = (V_j/N_j)^{1/3}$. The value g_{ij} is the total sum of interactions of all pairs of particles contained in volumes V_i and V_j, respectively. The interaction of a pair of particles is given as

$$P_{vdw} = -\frac{C}{d^6} \tag{5}$$

where d is the distance between a pair of particles, such that $d \gg R_M$ where R_M is the radius of the particles. Because the nanoparticles considered in this study are electrically neutral macromolecules with large surface area, a van der Waals potential with d^{-6} is used to describe molecular attraction between the aggregating particles.

Finally, we call the last term in eq 1 a smoothing potential. This term is computed as the difference between the number of particles in neighboring cells, with proportionality constant D. We introduce this term to prevent particles clustering into islands at the early stages of the simulation, owing to finite cell size. Consistent with this, we observe that the final deposit shape depends slightly on D, where this dependence decreases as cell size decreases.

The Hamiltonian in eq 1 is nondimensionalized by using the following characteristic scales:

$$R_0 = LR_0^* \qquad R_M = LR_M^* \qquad h_i = Lh_i^* \qquad \overline{d}_{ij} = L\overline{d}_{ij}^* \qquad a_0 = L^2 a_0^*$$

$$V_0 = L^3 V_0^* \qquad f_i = (\eta_m BL^2)\left(\frac{R_M}{L}\right)f_i^* \qquad g_{ij} = \hat{C}g_{ij}^*$$

where L is the characteristic length scale of a system, $\hat{C} = C/L^6$ is the characteristic energy scale of particle interaction. Setting $L = R_0$,

$$f_i^* = \sqrt{a_0^*}\sum_{k=i}^{n_0}(h_k^*)^{-\lambda} \qquad g_{ij}^* = \frac{1}{a_0^*\overline{d}_{ij}^{*4}} \tag{6}$$

where the superscript $(\ )^*$ denotes dimensionless values. Then Hamiltonian in eq 1 becomes

$$H_v = (\eta_m BR_0^2)R_M^*\sum_i f_i^* N_i - \hat{C}\sum_{\langle i,j\rangle} g_{ij}^* N_i N_j + \sum_{\langle i,j\rangle} D|N_i - N_j| \tag{7}$$

We scale H_v by the energy scale of the convection, $(\eta_m BR_0^2)R_M^*$; then the nondimensionalized Hamiltonian becomes

$$H_v^* = \sum_i f_i^* N_i - \frac{1}{Q}\sum_{\langle i,j\rangle} g_{ij}^* N_i N_j + \frac{1}{W}\sum_{\langle i,j\rangle} |N_i - N_j| \tag{8}$$

where we define dimensionless numbers Q and W as a ratio of convective potential to the particle interaction and a ratio of convective potential to the smoothing potential, respectively:

$$Q = R_M^*\left(\frac{\eta_m BR_0^2}{\hat{C}}\right) \qquad W = R_M^*\left(\frac{\eta_m BR_0^2}{D}\right) \tag{9}$$

2537

dx.doi.org/10.1021/jp4111844 | *J. Phys. Chem. B* 2014, 118, 2535–2543

In this study, we investigate the effect of Q on the deposit patterns with the energy W set at a value such that the effect of the smoothing potential is negligible compared to the convection and van der Waals potentials, respectively. The value Q describes the interplay between the convective transport and the aggregation of interacting particles. Roughly speaking, $Q \gg 1$ and $Q \ll 1$ represent convection-dominant and interaction-dominant cases, respectively. The ratio Q is proportional to the relative particle size R_M^* and the velocity constant B, whereas it is inversely proportional to the relative strength of particle interaction $\hat{C}$. The size of a droplet R_0 and the solvent viscosity η_m are fixed in our simulations. Note that because the evaporation-induced velocity $v(r,t)$ is roughly proportional to the evaporation rate,[11] the constant B in eq 3 can be viewed as a parameter to control evaporation rate.

The parameter Q explicitly partitions the energy between convection and interaction. However, other parameters in the model affect the energy. For example, the total number of particles N_{tot} affects the average interparticle distance d_{ij} and so affects the energy. Moreover, as we discuss in detail below, the total particle number N_{tot} has a separate role in the energy through the volume fraction of solute in a cell. Particle size R_M will also have an effect independent of its role in Q because it affects the solute volume fraction. Note that because d_{ij} reflects the distance between the centers of particles, it is independent of R_M.

Evolution by Monte Carlo Method. Monte Carlo methods have been widely used to obtain equilibrium configurations of Ising-type lattice models.[22,37] The lattice model is a straightforward energy model in which a Hamiltonian is defined at each configuration. The Monte Carlo method is used to compute the energy of the equilibrium configuration by using random numbers to allow for configurational changes that can both increase and decrease the energy. Because of the randomness inherent in the model, Monte Carlo methods are often applied to systems where evolution depends on diffusion, adsorption or aggregation.[28]

In the present study, we develop a Monte Carlo method to simulate the convective transport of particles owing to droplet evaporation, and their aggregation owing to weak interactions. The method consists of three interrelated parts: (1) modeling the evaporation of the droplet in the context of the MC simulation; (2) at every step in the process, using the Hamiltonian defined in eq 1 to find an equilibrium configuration; (3) describing a deposit phase as solute accumulates at the contact line.

We begin by modeling the evaporation process in the model. Unlike Rabani's model, the dynamics of evaporation is determined prior to determining the particle dynamics. We use the evaporation induced velocity fields (eq 3) as obtained by Deegan et al.[11] We allow evaporation of the droplet and subsequent decrease in droplet height by dividing the simulation into m_c Monte Carlo steps, with each MC step having N_{move} random trials using the Metropolis algorithm described below. Upon completion of each MC step we "evaporate" the droplet by decreasing the contact angle θ. Although one can derive an exact expression for $\theta(t)$ given the detailed evaporation rate,[11] we have chosen to simply let it decrease linearly with each MC step. Hence, with each MC step, we update the droplet height (and associated cell volumes) and solvent velocity.

In principle, the effective evaporation rate can be controlled by varying either N_{move} or m_c, or by changing the solute velocity

through B in eq 3. Increasing N_{move} increases the number of solute steps in a given MC cycle; hence more solute moves toward the contact line in that step and so the evaporation rate effectively increases. On the other hand, increasing m_c increases the MC time to fully dry the droplet and so decreases the effective evaporation rate. In practice, we take $N_{move} = N_{tot}$ so as to give each solute particle a chance to move during a given MC step. Also, we fix m_c to ensure that all solute moves to the contact line by the end of the simulation. This leaves B as the main control parameter, in the sense that with all else fixed, larger solute convection velocities, and hence higher Q, results from faster evaporation.

We next describe the MC dynamics at each step. These dynamics are simulated by using the Metropolis algorithm, which samples important configurations of the Boltzmann distribution in equilibrium. The evolution of a system is based on random walks: we attempt to move a randomly chosen particle at a cell i to the nearest neighbor j, resulting in $N_i \rightarrow N_i - 1$ and $N_j \rightarrow N_j + 1$. This attempt is accepted with a Metropolis probability, $p_{acc} = \exp(-\Delta H_\nu / k_B T)$, where ΔH_ν is the resulting change of the Hamiltonian in eq 1 due to the particle movement. In the model, particles execute a random walk on the lattice, biased by the Hamiltonian, and the total number of particles N_{tot} is conserved during each cycle.

As the Hamiltonian includes sums on the nearest neighbors, we use the following algorithm to determine these on the circular grid. The nearest neighbor of the circular grid system is defined as follows. The center point of a cell at a layer L_k is (r_c, θ_c) and is used as a position of the given cell. The two nearest neighbors in the r-direction are obtained by moving the point (r_c, θ_c) in the positive direction and the negative direction by dr. Then the positions become $(r_c + dr, \theta_c)$ and $(r_c - dr, \theta_c)$ located in the layers L_{k+1} and L_{k-1}, respectively. On the basis of these positions, we find the indexes i_{r+} and i_{r-}, which are already labeled over the lattice. On the other hand, the positions of the nearest neighbors in the θ direction are $(r_c, \theta_c + dr)$ and $(r_c, \theta_c - dr)$, which are both located in the L_k layer. The corresponding indexes will be simply $i + 1$ and $i - 1$, if the index of the given cell is i.

Finally, we describe our model of solute deposition. We introduce a constant, ϕ_{max}, such that when the volume fraction in a cell reaches ϕ_{max}, it is in the deposit phase. Note that the actual solute volume fraction in a cell is

$$\phi = N_i V_M / V_i$$

where N_i evolves by the MC simulation described above and V_i also evolves through the evaporation process as described above. The parameter V_M is the volume of one solute particle and so depends on particle size R_M. Once the volume fraction in a cell reaches ϕ_{max}, we do not accept any MC move to put more solute in that cell, though we do allow solute particles to leave the deposit cell and move to a surrounding (nondeposit) cell. Finally, the maximum number of particles at a cell i corresponding to ϕ_{max}, is computed as

$$N_{i,max} = \text{the integer rounded down from} \left(\phi_{max} \frac{V_i}{V_M} \right)$$

■ RESULTS AND DISCUSSION

Convective Ring-like Deposit Patterns. We investigate the characteristics of the patterns of noninteracting particles formed by the convection in the droplet. Without intermo-
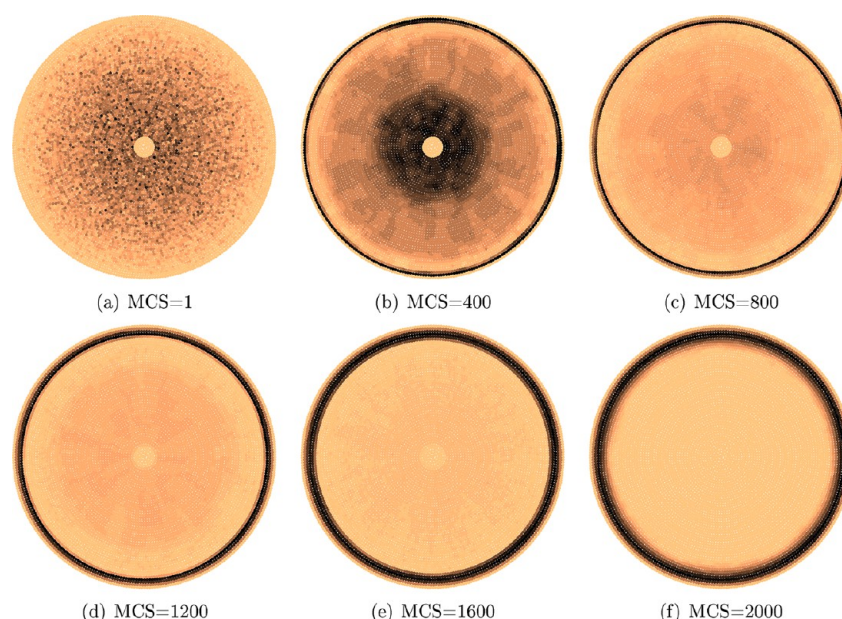
(a) MCS=1 (b) MCS=400 (c) MCS=800

(d) MCS=1200 (e) MCS=1600 (f) MCS=2000

Figure 3. Temporal evolution of the ring-like deposit from (a) to (f) with $N_{tot} = 40000$, $R_M^* = 2.5 \times 10^{-3}$, $B = 15$, $Q = \infty$, and $W = 37.5$. The nondimensional radius of the droplet is taken as 1.

lecular forces, the present model reduces to the model of solute transfer and deposition proposed by Deegan et al., and the ring-like patterns found by them can be reproduced.[11] Figure 3 shows the "temporal" evolution in MC steps of the ring-pattern formation. In particular, an initial distribution of particles and a typical final structure of a ring-like pattern are given in Figure 3a,f. The early behavior, shown in Figure 3b−e, is that particles near the contact line are deposited as a ring-shape, whereas particles inside a circular region move toward the contact line gradually. However, one layer of particles remains in the middle until the later stage, as shown in Figure 3d,e. This is attributed to the effect of the smoothing potential that prefers a flat configuration. Finally, all the particles are swept toward the contact line at the final time (Figure 3f). Note that in Figure 3f, and in all the plots hereafter, a nondimensional droplet radius of 1 is used. The cross-sectional profile of the final ring-like pattern is shown in Figure 4, where height is proportional to
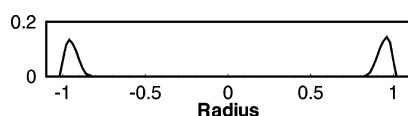

Figure 4. Profile of the particle deposition at the final time in Figure 3f where the height is defined by $N_{i,f}R_M^*$, where $N_{i,f}$ is the particle number of particles at a cell i at the final time.

the number of particles left at cells at the final time. It is readily observed from the figure that the slope of the deposit at the edge is greater than that at the interior, which is similar to the result experimentally found in Li et al.[13] In fact, the outer deposit is generated by particles that are initially transported from near to the contact line, and thus the slope is mainly determined by the initial contact angle θ_0. Particles then deposit at the lowered heights as the contact angle gradually decreases, hence so does the slope.

We can use our simulation to study how morphological features of the ring-like patterns are affected by different evaporation processes, i.e., diffusion limited evaporation and

spatially uniform evaporation. In our model, two different evaporation-induced velocities defined in eq 3 are implemented in the Hamiltonian in eq 1 while all other parameters are fixed. We then compare our results to the experimental results of Deegan and his co-workers.[11] In their experiments, the deposit patterns of two identical droplets were investigated under different conditions: one droplet evaporates at room temperature and the other evaporates on a substrate mounted on a pedestal and surrounded by a bath of water such that the level of the bath coincides with the base of a droplet. They reported that the former is a diffusion-limited case where the evaporation rate diverges at the contact line, and the latter is approximated as spatially uniform evaporation because the evaporation at the contact line is moderated by the water bath at the bottom.

Figure 5 shows the final ring-like patterns for two different evaporation rates with the number of particles N_{tot} of 7000 and the normalized size of particles R_M^* of 10^{-2}. In both cases, similar ring-like patterns are generated, but their thicknesses are quite different. For the diffusion-limited case in Figure 5a, the ring thickness of 4 in layer numbers is smaller than that of
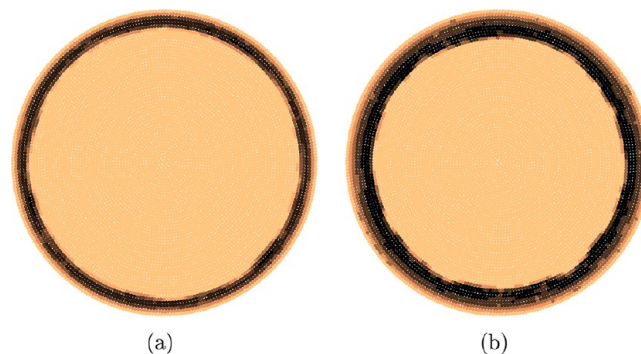

(a) (b)

Figure 5. Final ring-like patterns in the cases of (a) a diffusion-limited evaporation and (b) a spatially uniform evaporation, with $N_{tot} = 7000$, $R_M^* = 5 \times 10^{-3}$, $B = 10$, $Q = \infty$, and $W = 80$. The nondimensional radius of the droplet is taken as 1.

5.235 for the uniform-evaporation case in Figure 5b. In the diffusion limited evaporation case, particles near the contact line arrive and quickly deposit at the edge, whereas particles in the middle of the droplet take more time to arrive and deposit at the contact line. As such, particles deposit in the order of distance from the initial position to the edge line. At the final stage, all the particles are swept to the edge due to the large evaporation rate near the edge. This trend is observed in Figure 6 as a linear growth of the ring thickness in time ($\approx t$). On the
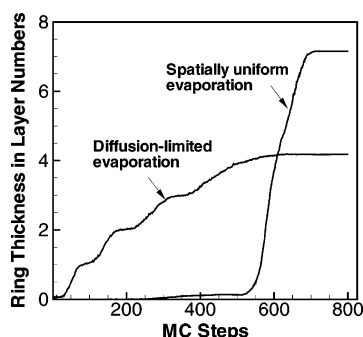

Figure 6. Temporal growths of ring thicknesses for two different evaporation cases: a diffusion-limited evaporation and a uniform evaporation.

other hand, in the case of uniform evaporation, the deposit grows relatively slowly due to the constant evaporation rate at the edge which is less than that in the diffusion-limited case. This trend is also observed in the growth rate in Figure 6 which shows an initial delay in deposition prior to sharp increase ($\approx t^2$).

Convective Deposit Patterns with Intermolecular Forces. In this section, the effect of particle interaction on the deposit patterns is elucidated by incorporating both convection and intermolecular forces into the model. We find that the interplay of the convection and the particle interaction can produce variations of the ring-like patterns. Figure 7 shows

the morphological variations as the ratio Q of the convection to interaction varies. We use the velocity in eq 3 associated with diffusion limited evaporation, though similar patterns arise with uniform evaporation. Other parameters are as given in the figure. It is observed from Figure 7 that as the value of Q decreases, a morphology with a wave-like pattern along the contact line appears first (Figure 7b), followed by disconnected finger-like patterns at the edge (Figure 7c). As Q is further decreased, some particles are left in the middle of the substrate as shown in Figure 7d. These leftover particles are not transported to the contact line by the convective flow owing to the strong particle interactions. When the particle interaction completely dominates the convection, particles do not move toward the edge but remain on the substrate as small dispersed island-like patterns (Figure 7e,f). The more islands in the middle of the substrate can be observed in Figure 7f compared to in Figure 7e owing to the relatively smaller value of Q in Figure 7f. This implies that particles aggregate within short distances due to the stronger interaction.

It is interesting to qualitatively compare these results to the experiments of dendrimer–alcohol solution by Li et al.[14] They found that a hexanol-based solution leaves a ring-like pattern with the additional distribution of dendrimer deposit islands in the interior, whereas a pentanol-based solution leaves a ring-like pattern with a clear interior.[14] Hexanol evaporates 3 times slower than pentanol, implying that relative convective force in the hexanol-based solution is weaker than that in the pentanol-based solution. As in our simulations, the low convective force (low Q) that would be associated with the slow evaporation rate of hexanol leads to dendrimer islands remaining in the interior of the droplet after evaporation.

Wave-like Patterns. As shown in Figure 7, wave-like patterns appear in an intermediate regime between ring patterns and island patterns, where convection and interaction, respectively, dominate. To better understand the wave-like patterns, their evolution is shown in Figure 8 for increasing numbers of MC steps. In general, the evolution is similar to that
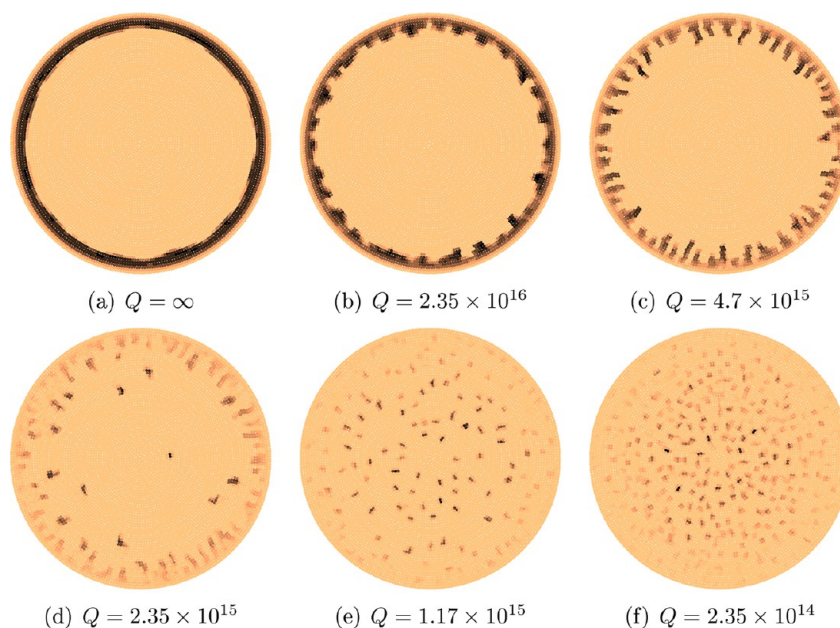

$(a)\ Q = \infty$　　　　$(b)\ Q = 2.35 \times 10^{16}$　　　　$(c)\ Q = 4.7 \times 10^{15}$

$(d)\ Q = 2.35 \times 10^{15}$　　　$(e)\ Q = 1.17 \times 10^{15}$　　　$(f)\ Q = 2.35 \times 10^{14}$

Figure 7. Several different deposit patterns for different Q with $N_{tot} = 5000$, $R_M^* = 6.25 \times 10^{-3}$, $B = 15$, and $W = 94$. The nondimensional radius of the droplet is taken as 1.

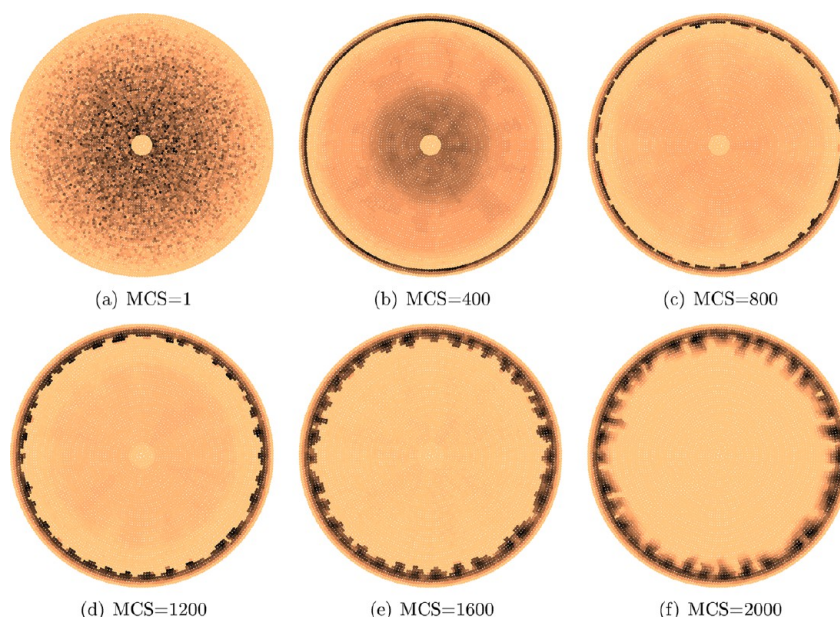**Figure 8.** Temporal evolution of the formation of a typical wave-like deposit structure with $N_{tot} = 56000$, $R_M^* = 2.5 \times 10^{-3}$, $B = 15$, $Q = 9.4 \times 10^{17}$ and $W = 37.5$. The nondimensional radius of the droplet is taken as 1.
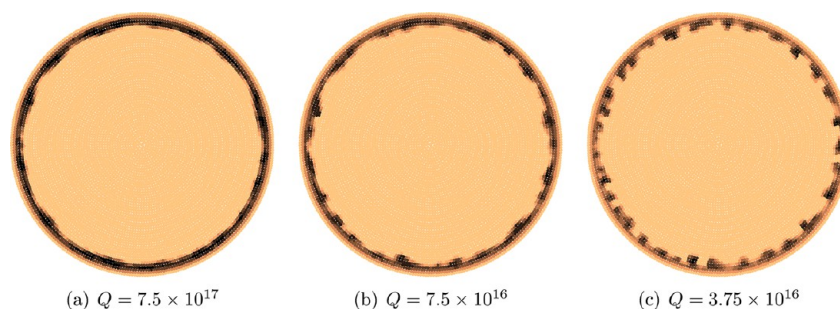

Figure 9. Wave-like deposit patterns for different Q with $N_{tot} = 5000$, $R_M^* = 5 \times 10^{-3}$, $B = 15$, and $W = 75$. The nondimensional radius of the droplet is taken as 1.

of the ring patterns shown in Figure 3. After a thin ring forms (Figure 8b), small scale waves start to appear along the contact line owing to particle interaction and the higher concentration of particles. However, particles in the interior of the droplet have not all been transferred toward the edge. The waviness of the deposit increases in Figure 8c−e as these interior particles convect from the interior of the droplet to the contact line. More, it appears that once the wave-like pattern is formed, it does not significantly change in time (as might be expected from surface energy, for example).

Figure 9 shows how wave-like patterns depend on the ratio Q, with other parameters fixed. It is readily observed that the wavenumber increases with decreasing Q. These results agree qualitatively with the results of Li et al.[14] in the following sense. As already discussed, Li et al. used both hexanol and pentanol as solvents, where hexanol has a lower evaporation rate than pentanol, hence lower convective velocity and smaller Q. Consistent with Figure 9, they also found that the hexanol based solution left patterns with higher wavenumbers than deposits from pentanol based solution.

Finally, as mentioned previously, variations in N_{tot} and R_M^* affect the results through their role in the deposition process, separate from their role in Q. Figure 10 shows the approximate (hand-computed) wavenumber of the wavy pattern as a function of the dimensionless solute size R_M^*. We plot for Q
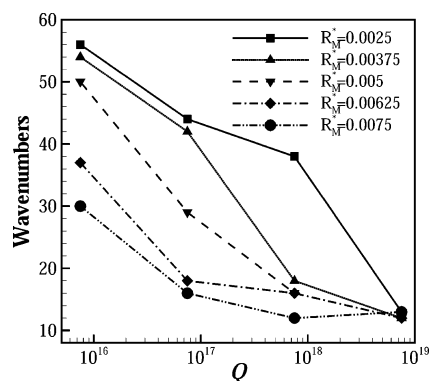

Figure 10. Wavenumbers of deposit patterns as a function of Q for different R_M^* with $N_{tot} = 5000$, $B = 15$, and $W = 75$.

between $O(\sim 10^{16})$ and $O(\sim 10^{19})$, which is roughly the range for which patterns are clearly wave-like. We observe, consistent with Figure 9, that wavenumber decreases with Q for all R_M^*. However, at a given value of Q, we observe that the wavenumber decreases as the particle size increases. This appears to be a result of the fact that as R_M^* increases, fewer particles are needed to form a deposit in a given volume. Hence we observe that the deposit ring thickness, before a wavy

structure forms, increases as R_M^* increases, and the pattern itself stays closer to the ring-like shape. We believe that this is associated with a decrease in mobility of solute particles at higher volume fractions, as there is limited "space" to add particles in cells that are close to ϕ_{max}. This seems to effectively limit the waviness of the resulting patterns. Note that as Q decreases below $O(\sim 10^{16})$, patterns change to finger-like patterns and eventually to isolated islands, as discussed above (Figure 7c,d). On the other hand, when Q is larger than $O(\sim 10^{19})$, the effect of particle interaction reduces and deposit morphology becomes close to ring patterns.

A similar result can be found by changing N_{tot} at fixed R_M^* (Figure 11). Here we again observe at any given N_{tot} the
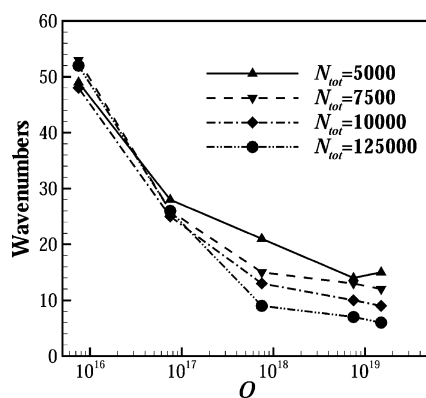

Figure 11. Wavenumbers of deposit patterns as a function of Q for different N_{tot} with $R_M^* = 5 \times 10^{-3}$, $B = 15$, and $W = 75$.

wavenumber increases with decreasing Q, i.e., as particle interaction increases relative to convection. However, for fixed Q at a range between the orders of $O(\sim 10^{17})$ and $O(\sim 10^{19})$, wavenumber decreases as N_{tot} increases, despite the fact that the interparticle distance decreases, hence particle interaction increases, as N_{tot} increases. As with the previous case, we observe that ring thickness increases as N_{tot} increases, and that the wave-like pattern stays closer to a ring-like shape owing to the low mobility of particles near the deposit phase. Finally, we remark that these observations agree qualitatively with the results of Li et al., who find that at higher dendrimer concentrations, hence thicker rings, the wavenumber of the wave-like pattern decreases.[14]

CONCLUSION

In the present study, we have discussed the formation of wave-like patterns of particles seeded in a drying droplet on a substrate. For this purpose, a new lattice gas model was developed to examine the deposit patterns driven by the interplay of evaporation-induced convection and pairwise interacting particles. The model was first used to reveal the characteristics of the "coffee ring" patterns induced by convection only. As also shown by Deegan et al.,[11] different convective velocities induced by different evaporation rates and a fixed contact line result in different ring thicknesses.

When particle–particle interactions are considered, the system energy depends on the ratio of convection and particle interaction, as given by the dimensionless parameter Q. As expected, the characteristics of wave-like patterns depend critically on Q. We find coffee-ring patterns at large Q, i.e., when convection dominates particle interaction. As Q decreases and particle interaction strengthens, we observe wave-like

patterns as particles starts to aggregate at the contact line. The wavelength of these wave-like patterns increases as Q decreases, and also as R_M^* decreases. These results agree qualitatively with the patterns observed by Li et. al in their experiments on dendrimer deposits in evaporating droplets.[13,14] For even smaller Q, we find island-like patterns as particle interaction starts to dominate convection. Finally, we find transition patterns such as finger-like patterns or mixtures of both wave-like and island-like patterns for Q between values associated with the clear wave-like and island-like patterns.

AUTHOR INFORMATION

Corresponding Authors
*C. S. Yoo: e-mail, csyoo@unist.ac.kr.
*P. H. Leo: e-mail, phleo@umn.edu.
Notes
The authors declare no competing financial interest.

REFERENCES

(1) Park, J.; Moon, J. Control of Colloidal Particle Deposit Patterns within Picoliter Droplets Ejected by Ink-Jet Printing. *Langmuir* **2006**, *22*, 3506−3513.

(2) Sorrell, C. D.; Carter, M.; Serpe, M. J. A "Paint-on" Protocol for the Facile Assembly of Uniform Microgel Coatings for Color Tunable Etalon Fabrication. *Appl. Mater. Interfaces* **2011**, *3*, 1140−1147.

(3) Perelaer, J.; Smith, P. J.; van den Bosch, E.; van Grootel, S. S.; Ketelaars, P. H. J. M.; Schubert, U. S. The Spreading of Inkjet-Printed Droplets with Varying Polymer Molar Mass on a Dry Solid Substrate. *Macromol. Chem. Phys.* **2009**, *210*, 495−502.

(4) Han, W.; Lin, Z. Learning from "Coffee Rings" Ordered Structures Enabled by Controlled Evaporative Self-Assembly. *Angew. Chem., Int. Ed.* **2012**, *51*, 1534−1546.

(5) Singh, M.; Haverinen, H. M.; Dhagat, P.; Jabbour, G. E. Inkjet Printing Process and Its Applications. *Adv. Mater.* **2010**, *22*, 673−685.

(6) Kawase, T.; Shimoda, T.; Newsome, C.; Sirringhaus, H.; Friend, R. K. Inkjet Printing of Polymer Thin Film Transistors. *Thin Solid Films* **2003**, *438−439*, 279−287.

(7) Wolfe, D. B.; Love, J. C.; Paul, K. E.; Chabinyc, M. L.; Whitesides, G. M. Fabrication of Palladium Based Microelectronic Devices by Microcontact Printing. *Appl. Phys. Lett.* **2002**, *80*, 2222−2224.

(8) Liu, Y.; Cui, T.; Varahramyan, K. All-Polymer Capacitor Fabricated with Inkjet Printing Technique. *Solid-State Electron.* **2003**, *47*, 1543−1548.

(9) Nohria, R.; Khillan, R. K.; Su, Y.; Dikshit, R.; Lvov, Y. Humidity Sensor Based on Ultrathin Polyaniline Film Deposited Using Layer-by-Layer Nano-Assembly. *Sens. Actuators, B* **2006**, *114*, 218−222.

(10) Heller, M. J. DNA Microarray Technology: Devices, Systems, and Applications. *Annu. Rev. Biomed. Eng.* **2002**, *4*, 129−153.

(11) Deegan, R. D.; Bakajin, O.; Dupont, T. F.; Huber, G.; Nagel, S. R.; Witten, T. A. Contact Line Deposits in an Evaporating Drop. *Phys. Rev. E* **2000**, *62*, 756−765.

(12) Deegan, R. D.; Bakajin, O.; Dupont, T. F.; Huber, G.; Nagel, S. R.; Witten, T. A. Capillary Flow as the Cause of Ring Stains from Dried Liquid Drops. *Nature* **1997**, *389*, 827−829.

(13) Li, F.-I.; Thaler, S. M.; Leo, P. H.; Barnard, J. A. Dendrimer Pattern Formation in Evaporating Drops. *J. Phys. Chem. B* **2006**, *110*, 25838−25843.

(14) Li, F.-I.; Leo, P. H.; Barnard, J. A. Dendrimer Pattern Formation in Evaporating Drops: Solvent, Size, and Concentration Effects. *J. Phys. Chem. B* **2008**, *112*, 14266−14273.

(15) Hu, H.; Larson, R. G. Marangoni Effect Coffee-Ring Depositions. *J. Phys. Chem. B* **2006**, *110*, 7090−7094.

(16) Denkov, N.; Velev, O.; Kralchevsky, P.; Ivanov, I.; Yoshimura, H.; Nagayama, K. Mechanism of Formation of Two-Dimensional Crystals from Latex Particles on Substrates. *Langmuir* **1992**, *8*, 3183−3190.

(17) Yunker, P. J.; Still, T.; Lohr, M. A.; Yodh, A. Suppression of the Coffee-Ring Effect by Shape-Dependent Capillary Interactions. *Nature* **2011**, *476*, 308−311.

(18) Yunker, P. J.; Lohr, M. A.; Still, T.; Borodin, A.; Durian, D.; Yodh, A. Effects of Particle Shape on Growth Dynamics at Edges of Evaporating Drops of Colloidal Suspensions. *Phys. Rev. Lett.* **2013**, *110*, 035501 (1−5).

(19) Sommer, A. P.; Gheorghiu, E.; Cehreli, M.; Mester, A. R.; Whelan, H. T. Biosensor for Detection of Nanobacteria in Water. *Cryst. Growth Des.* **2006**, *6*, 492−497.

(20) Shen, X.; Ho, C.-M.; Wong, T.-S. Minimal Size of Coffee Ring Structure. *J. Phys. Chem. B* **2010**, *114*, 5269−5274.

(21) Cheng, S.; Grest, G. S. Molecular Dynamics Simulations of Evaporation-Induced Nanoparticle Assembly. *J. Chem. Phys.* **2013**, *138*, 064701.

(22) Rabani, E.; Relchman, D. R.; Gelssler, P. L.; Brus, L. E. Drying-Mediated Self-Assembly of Nanoparticles. *Nature* **2003**, *426*, 271−274.

(23) Sztrum, C. G.; Hod, O.; Rabani, E. Self-Assembly of Nanoparticles in Three-Dimensions: Formation of Stalagmites. *J. Phys. Chem. B* **2005**, *109*, 6741−6747.

(24) Hod, O.; Rabani, E. A Coarse-Grained Model for a Nanometer-Scale Molecular Pump. *Proc. Natl. Acad. Sci. U. S. A.* **2003**, *100*, 14661−14665.

(25) Sztrum-Vartash, C. G.; Rabani, E. Lattice Gas Model for the Drying-Mediated Self-Assembly of Nanorods. *J. Phys. Chem. C* **2010**, *114*, 11040−11049.

(26) Kletenik-Edelman, O.; Ploshnik, E.; Salant, A.; Shenhar, R.; Banin, U.; Rabani, E. Drying-Mediated Hierarchical Self-Assembly of Nanoparticles: A Dynamical Coarse Grained Approach. *J. Phys. Chem. C* **2008**, *112*, 4498−4506.

(27) Yosef, G.; Rabani, E. Self-Assembly of Nanoparticles into Rings: A Lattice-Gas Model. *J. Phys. Chem. B* **2006**, *110*, 20965−20972.

(28) Vancea, I.; Thiele, U. Front Instabilities in Evaporatively Dewetting Nanofluids. *Phy. Rev. E* **2008**, *78*, 041601 (1−15).

(29) Lee, S. H.; Yoo, P. J.; Kwon, S. J.; Lee, H. H. Solvent Driven Dewetting and Rim Instability. *J. Chem. Phys.* **2004**, *121*, 4346−4351.

(30) Brochard-Wyart, F.; Redon, C. Dynamics of Liquid Rim Instability. *Langmuir* **1992**, *8*, 2324−2329.

(31) *Asano, Pattern Formation by Rim Instability in Dewetting Polymer Thin Films*; American Chem. Society: Washington, DC, 2004; Chapter 15.

(32) Gabriele, S.; Coppee, S.; Reiter, G.; Damman, P. On the Mechanics of Rim Instabilies in Viscoelastic Polymer Thin Films. *Eur. Phys. J. Special Topics* **2009**, *166*, 55−61.

(33) Xu, L.; Shi, T.; Dutta, P. K.; An, L. Rim Instability by Solvent Induced Dewetting. *J. Chem. Phys.* **2007**, *127*, 144704 (1−7).

(34) Choi, S.; Newby, B. Z. Dynamic Contact Angle in Rim Instability of Dewetting Holes. *J. Chem. Phys.* **2006**, *124*, 054702 (1−6).

(35) Newman, M. E. J.; Barkema, G. T. *Monte Carlo Methods in Statistical Physics*; Oxford University Press: Oxford, U.K., 1998.

(36) Kim, H. S.; Park, S. S. Compuational Approach to Drying a Nanoparticle-Suspended Liquid Droplet. *J. Nanopart. Res.* **2011**, 59−68.

(37) Chandler, D. *Introduction to Modern Statistical Mechanics*; Oxford University Press;: Oxford, U.K., 1987.

2543

dx.doi.org/10.1021/jp4111844 | *J. Phys. Chem. B* 2014, 118, 2535−2543